

## Critical strain for Sn incorporation into spontaneously graded Ge/GeSn core/shell nanowires

Albani, Marco; Assali, Simone; Verheijen, Marcel A.; Koelling, Sebastian; Bergamaschini, Roberto; Pezzoli, Fabio; Bakkers, Erik P.A.M.; Miglio, Leo

**DOI**

[10.1039/c7nr09568f](https://doi.org/10.1039/c7nr09568f)

**Publication date**

2018

**Document Version**

Final published version

**Published in**

Nanoscale

**Citation (APA)**

Albani, M., Assali, S., Verheijen, M. A., Koelling, S., Bergamaschini, R., Pezzoli, F., Bakkers, E. P. A. M., & Miglio, L. (2018). Critical strain for Sn incorporation into spontaneously graded Ge/GeSn core/shell nanowires. *Nanoscale*, 10(15), 7250-7256. <https://doi.org/10.1039/c7nr09568f>

**Important note**

To cite this publication, please use the final published version (if applicable). Please check the document version above.

**Copyright**

Other than for strictly personal use, it is not permitted to download, forward or distribute the text or part of it, without the consent of the author(s) and/or copyright holder(s), unless the work is under an open content license such as Creative Commons.


**Takedown policy**

Please contact us and provide details if you believe this document breaches copyrights. We will remove access to the work immediately and investigate your claim.



Cite this: *Nanoscale*, 2018, **10**, 7250

## Critical strain for Sn incorporation into spontaneously graded Ge/GeSn core/shell nanowires

Marco Albani, <sup>a</sup> Simone Assali, <sup>†b</sup> Marcel A. Verheijen, <sup>b,c</sup> Sebastian Koelling, <sup>b</sup> Roberto Bergamaschini, <sup>a</sup> Fabio Pezzoli, <sup>a</sup> Erik P. A. M. Bakkers <sup>b,d</sup> and Leo Miglio <sup>\*a</sup>

We address the role of non-uniform composition, as measured by energy-dispersive x-ray spectroscopy, in the elastic properties of core/shell nanowires for the Ge/GeSn system. In particular, by finite element method simulations and transmission electron diffraction measurements, we estimate the residual misfit strain when a radial gradient in Sn and a Ge segregation at the nanowire facet edges are present. An elastic stiffening of the structure with respect to the uniform one is concluded, particularly for the axial strain component. More importantly, refined predictions linking the strain and the Sn percentage at the nanowire facets enable us to quantitatively determine the maximum compressive strain value allowing for additional Sn incorporation into a GeSn alloy. The progressive incorporation with increasing shell thickness, under constant growth conditions, is specifically induced by the nanowire configuration, where a larger elastic relaxation of the misfit strain takes place.

Received 22nd December 2017,

Accepted 10th March 2018

DOI: 10.1039/c7nr09568f

rsc.li/nanoscale

## Introduction

In the quest for direct bandgap group IV semiconductors, GeSn alloys provide a fair flexibility to independently engineer the bandgap and lattice parameters on a broad range.<sup>1–3</sup> The direct growth of GeSn on a Si substrate is an important advantage to achieve scalable and cost-effective Si photonics operating at mid-IR wavelengths of 2–5  $\mu\text{m}$ .<sup>4</sup>

The large difference in lattice parameters between Sn and Ge leads to a strain exceeding 15%,<sup>5</sup> resulting in the formation of a high density of defects.<sup>6,7</sup> In addition, compressive strain in the GeSn layer increases the percentage of Sn required to observe an indirect-to-direct bandgap transition.<sup>2,6,8</sup> Therefore, great care needs to be exercised in optimizing the material composition to fabricate high-efficiency mid-IR opto-electronic devices.<sup>5,9</sup> The main challenge in the growth of GeSn alloys originates from the extremely low equi-

librium solubility of Sn in Ge ( $\sim 1\%$ ).<sup>10</sup> The difference in surface free energy, combined with the extremely low solubility, leads to Sn segregation and precipitation on the surface during growth.<sup>11–14</sup> In order to achieve Sn incorporation at concentrations above 10–12%, without segregation, the common strategy is to use out-of-equilibrium deposition methods<sup>15,16</sup> and to maximize strain relaxation.<sup>7,13,14</sup> Indeed, the incorporation kinetics is expected to be very sensitive to the compressive strain value at the surface, as for the “pulling effect” already reported for AlGaIn.<sup>17</sup>

In the case of films on Ge, the two main approaches are to increase the compliance of the Ge buffer,<sup>2,6</sup> or to manage the progressive strain by plastic relaxation.<sup>18</sup> Step-graded GeSn layers with Sn contents up to 16% were demonstrated for this latter case.<sup>19</sup> However, plastic relaxation by different types of dislocations is a spontaneous, difficult to control mechanism, and the threading arms easily affect the top layers.

For these reasons, a core/shell Ge/GeSn nanowire (NW) structure is a promising solution,<sup>20,21</sup> as fully elastic strain relaxation can be achieved, both due to the highly elastic compliance of a thin Ge core and to the effect of the free facets at the sidewalls. In particular, in ref. 20 a spontaneous grading of Sn concentration beyond 12% with increasing shell thickness was observed and suggested to affect strain relaxation.

Reasonably, the increased Sn content could be related to an enhancement in strain relaxation, as recently observed in the

<sup>a</sup>L-NESS and Dept. of Materials Science, University of Milano-Bicocca, Milano 20125, Italy. E-mail: leo.miglio@unimib.it

<sup>b</sup>Dept. of Applied Physics, Eindhoven University of Technology, Eindhoven 5600 MB, The Netherlands

<sup>c</sup>Philips Innovation Laboratories Eindhoven, High Tech Campus 11, 5656AE Eindhoven, The Netherlands

<sup>d</sup>Kavli Institute of Nanoscience, Delft University of Technology, Delft 2600 GA, The Netherlands

<sup>†</sup>Present address: Dept. of Engineering Physics, Polytechnique Montréal, C. P. 6079, Succ. Centre-Ville, Montréal, Québec H3C 3A7, Canada.

growth of Sn-rich bulk GeSn layers.<sup>22</sup> It is the goal of our work to shed light on the complex interplay between these two effects. In particular, we show how the core/shell NW structure has a favourable effect on Sn incorporation, thanks to enhanced elastic relaxation at growing shell thickness.

The starting point for our analysis is to accurately characterize the residual strain in the NW. Experimentally, this is not a trivial task, as the order of magnitude of typical strain values ( $10^{-3}$ ) is close to the accuracy limit of Transmission Electron Microscopy (TEM). Moreover, strain is expected to vary locally due to non-uniform Sn distribution in the shell, investigated by dedicated Energy-Dispersive X-ray (EDX) measurements. In addition to the Sn radial gradient, we observe the segregation of Ge along a sunburst-like geometry, aligned to the edges between the NW free facets, due to growth kinetic effects.<sup>23</sup>

Here, we pursue a theoretical approach to quantify the elastic relaxation and to evaluate the residual misfit strain. More precisely, we solve the mechanical equilibrium equations by the Finite Element Method (FEM) to compute the actual strain field in a realistic three-dimensional NW morphology, including all compositional features. The results are compared to improved TEM measurements, made possible by an internal calibration method.

Finally, a critical analysis of the reported results enables us to determine quantitatively the maximum strain allowing for incremental Sn incorporation.

## Results and discussion

Ge/Ge<sub>0.895</sub>Sn<sub>0.105</sub> core/shell NWs were grown in a chemical vapor deposition (CVD) reactor using germane (GeH<sub>4</sub>), tin chloride (SnCl<sub>4</sub>), and hydrogen chloride (HCl) as precursors, as described in ref. 20. Arrays of Ge NWs with 50 nm diameter were grown on a Ge (111) wafer for 2 h at 320 °C, followed by GeSn shell growth for 5 h at 300 °C using a GeH<sub>4</sub>/SnCl<sub>4</sub> precursor ratio of 740. The EDX compositional map in the hexagonal cross-section of the NW, as defined by {112} facets, is reported in Fig. 1a. The presence of Sn-poor sunburst-like stripes, developing radially from the core to the vertices of the hexagonal shell, is well evident by the colour contrast. In the remaining portion of the shell a composition of 10.5% Sn is estimated by averaging within the yellow rectangle shown in Fig. 1b. More precisely, a gradual increase of the Sn content is recognized while moving toward the outer surface, as illustrated in the line profile along the <112> direction in Fig. 1c. In addition, no clustering or local precipitation of Sn is observed<sup>20</sup> indicating limited diffusion of Sn during growth. Despite its small magnitude, the radial compositional change across the shell from 8% to 10.5% has a strong effect on the strain relaxation and on the electronic band structure of GeSn.<sup>5,8,24</sup>

In order to characterize the strain of the core/shell NWs of Fig. 1a, the mechanical equilibrium problem is solved numerically by FEM (see the Methods section for details). As observed experimentally, the composition in the GeSn shell is varied lin-

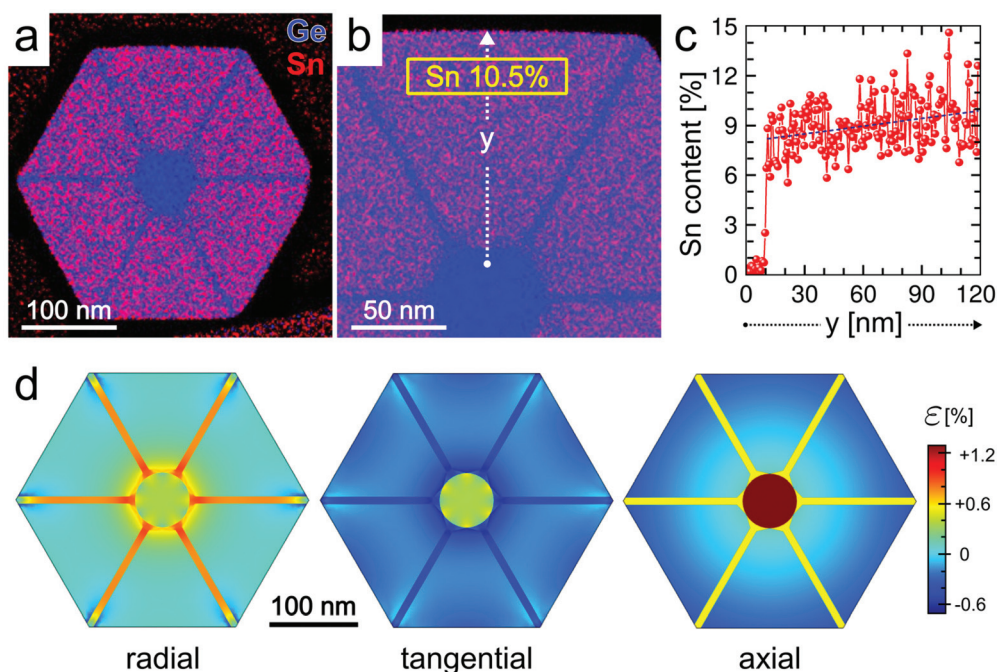


**Fig. 1** (a) Cross-sectional EDX compositional map of a Ge/Ge<sub>0.895</sub>Sn<sub>0.105</sub> core/shell NW (from ref. 20). The core radius is 30 nm and the shell thickness is  $\sim 110$  nm. A nominal shell composition of  $10.5 \pm 0.5\%$  in Sn is estimated by averaging the EDX signal within the yellow rectangle reported in the magnified view in panel (b). (c) Variation of the Sn content along the NW radius "y" showing the progressive increase of the Sn amount in the shell (dashed tendency line). (d) Color maps of the radial, tangential and axial components of the strain field, as computed by FEM. A linear composition gradient from 8% to 10.5% Sn and 5% Sn stripes along the hexagon vertices are assumed in order to match the experiments.

**Table 1** Average strain values from FEM calculations, for the case including the Sn composition gradient and sunburst-like stripes as in Fig. 1d and the case of a shell with a uniform composition of 9.6%. The averages are computed in the core volume and in the surrounding shell volume by considering the central portion of the NW, as long as  $\frac{1}{4}$  of the total NW length. The volume of the sunburst-like stripes is excluded from the averages

		Radial	Tangential	Axial [111]
Composition gradient + sunburst stripes	Shell	0.12%	-0.19%	-0.13%
	Core	0.38%	0.37%	1.33%
Uniform composition	Shell	0.12%	-0.06%	-0.06%
	Core	0.39%	0.39%	1.39%

early along the shell radius from 8% to 10.5% Sn (which corresponds to an average composition in the shell of 9.6%) and Sn-poor sunburst stripes are considered. The solution of the strain field computed for this configuration is reported by the colour maps in Fig. 1d for the radial, tangential, and axial components, representative of the NW axial symmetry. Table 1 reports the values of the strain components obtained by averaging the FEM results in the GeSn shell volume (excluding the sunburst stripes from the average) and in the Ge core volume. The tangential and axial strain fields are compressive within the shell, due to the lattice misfit between GeSn and Ge. According to Poisson's ratio, the radial strain field, which is essentially perpendicular to the free surface, is tensile.

In Table 1, the values of strain components are also reported for the hypothetical case of a shell with a fully uniform composition equal to the average of 9.6% Sn. Despite the small values, the residual strain for axial and tangential components is clearly larger for the realistic composition profile. In particular, the sunburst structure, due to the lower Sn content, contrasts the tendency of the shell to expand axially and radially, thus providing an additional structural stiffness to the shell, while only a small part of the strain can be transferred to the sunburst structure along the tangential direction. Our FEM prediction of the average compressive strain in the shell is nearly one order of magnitude smaller than the rough estimation of 0.7% in ref. 20. An explanation for such a large difference can be traced back to two issues. The first one is that, in ref. 20, the estimation of the residual strain on the basis of the experimental lattice parameter was made under the assumption of uniform Sn distribution corresponding to maximum incorporation (*i.e.* 13%). The second one comes from the inaccuracy in the measurements of the lattice parameter, resulting from the calibration method considered there. Hence, more refined diffraction measurements are needed to resolve this discrepancy.

An experimental measurement of the NW strain is challenging. Indeed, a Geometrical Phase Analysis (GPA)<sup>25,26</sup> is not suitable for our samples as it requires a reference area within the same field of view, that is not available in our 3D core/shell geometry. Alternatively, by analysing the electron diffraction (ED) patterns acquired in TEM measurements, we estimate the

average values of different strain components in the NW. We image the NW along the  $\langle 110 \rangle$  zone axis to evaluate the strain in the  $\langle 111 \rangle$  and  $\langle 200 \rangle$  directions. To reach the required measurement precision, a material enabling the calibration of the ED pattern is needed in the area of interest. For this reason, Pt nanoparticles are deposited on the supporting holey carbon film prior to depositing the wires on the film and are used for calibration. An external calibration procedure can be performed by probing areas without an overlap between the wire and the substrate, as shown in Fig. 2a. In this case, we separately acquire the poly-crystalline ring patterns from the Pt nanoparticles alone (see Fig. 2b) and the NW spots (see Fig. 2c), using the former as a reference for the latter. More efficiently, and more accurately, an internal calibration approach (see Fig. 2d) can be exploited by collecting the ED signal of the Pt nanoparticles directly superimposed on the NW diffraction patterns (see Fig. 2e). We then estimate the strain along the NW [111] axis, and along the  $\langle 111 \rangle$  and  $\langle 200 \rangle$  directions, inclined at an angle of  $70^\circ$  and  $54^\circ$ , respectively (see Fig. 2f).

From the ED patterns, we retrieve one single value for both core and shell, but we assume that each ED spot is actually representative just for the shell, as it comprises the major part of the volume. Moreover, in each measurement, we see a projected ED pattern of both the centre and edges simultaneously. However, we expect that the lattice parameter is different from the centre of the nanowire to the edges, mainly due to the variation in Sn composition. Therefore, we can just provide average values and this limits the accuracy. The absolute error of the measured lattice spacing is  $0.01 \text{ \AA}$ . To obtain this high accuracy, apart from the internal calibration using Pt nanoparticles, also a correction for the anisotropy of the magnification within the image is taken into account. The strain is then obtained by comparing the measured lattice parameter ( $a_{\text{ED}}$ ) with the unstrained value ( $a_{\text{lit}}$ ), given by a corrected version of Vegard's law (see the Methods section for details), as  $(a_{\text{ED}} - a_{\text{lit}})/a_{\text{lit}}$ , assuming an average 9.6% Sn composition. From this formula, *e.g.*, it can be concluded that an error of  $0.01 \text{ \AA}$  on the lattice spacing corresponds to a variability of about 0.3% in strain.

The experimental strain values are reported in Table 2 and compared with the FEM results, obtained by projecting the strain tensor along the same three orientations analysed by TEM: axial [111],  $\langle 111 \rangle$  and  $\langle 200 \rangle$ .

At a glance, it is notable how experimental measurements by different calibration methods, and even the two independent samples tested by internal calibration, are affected by a large variability, probably due to the complexity of the experimental setup. Still, they indicate that the actual value for the strain is smaller than 0.7%, closer to the FEM predictions, which prove to be quite an essential tool for a more quantitative analysis of the NW strain. In particular, it is unlikely that the  $\langle 111 \rangle$  and  $\langle 200 \rangle$  strain components are much larger than the tangential one, leading to an internal coherence with our calculations.

An independent confirmation of the accuracy of our strain analysis is given by comparison with the optical properties of

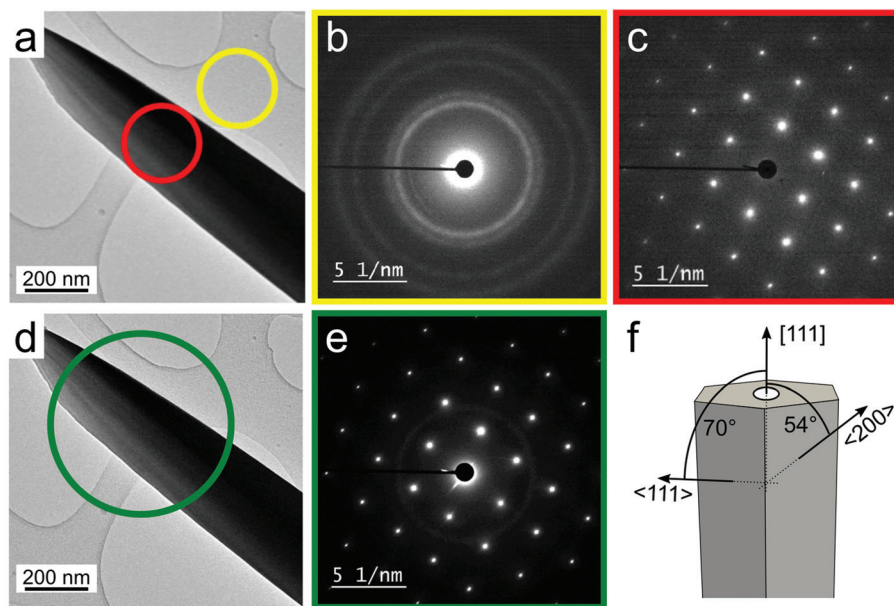


**Fig. 2** (a) Bright field TEM image of a GeSn NW disposed on the TEM grid for the strain measurement by external calibration, separating (b) the diffraction pattern of the Pt nanoparticles alone and (c) the NW diffraction pattern. The circles represent the diameters and positions of the selected-area electron diffraction apertures. (d) Bright field TEM image of the GeSn NW on the TEM grid for strain measurement by internal calibration, superimposing the signals from both the Pt nanoparticle and the NW in the diffraction pattern (e). The sample is the same as described in Fig. 1. (f) Schematic representation of the directions along which the strain is determined.

**Table 2** Comparison of the strain values obtained by FEM calculations and TEM measurements. FEM results are reported for both the case of a shell with uniform composition of 9.6% and the case including composition gradient and sunburst stripes, as in Table 1. The strain tensor is projected along the axial  $[111]$ ,  $\langle 111 \rangle$  and  $\langle 200 \rangle$  directions to compare with TEM data and averaged on the same shell volume as in Table 1. TEM data are acquired by both external and internal calibration techniques. In the latter case, measurements from two different NWs from the same sample (labelled as NW1 and NW2) are reported to show the uncertainty of the strain data, due to the 0.3% inaccuracy in the strain value derived from the electron diffraction patterns

		Axial $[111]$	$\langle 111 \rangle$	$\langle 200 \rangle$
FEM	Uniform composition	-0.06%	-0.03%	-0.03%
	Composition gradient + sunburst stripes	-0.13%	-0.05%	-0.07%
TEM	NW 1 external calibration	-0.46%	-0.46%	-0.56%
	NW 1 internal calibration	-0.55%	-0.03%	-0.31%
	NW 2 internal calibration	-0.16%	0.45%	-0.03%

NWs with the same composition.<sup>20</sup> By applying the deformation potential theory,<sup>2,27</sup> we expect a direct gap energy at  $\sim 0.549$  eV for a NW with an average Sn content of 9.6%, and a compressive in-plane strain (average of the tangential and radial components) of 0.04% in the cross-section, as predicted by the FEM analysis. Such a result is in nice agreement with the absorption data reported in ref. 20 for Ge/Ge<sub>0.895</sub>Sn<sub>0.105</sub> core/shell NWs. Notably, the radial gradients in the strain and Sn content unveiled by our analysis suggest that the radiative

recombination in NWs featuring a sunburst-like structure can predominantly occur in the outer portion of the shell, which has a lower bandgap as it is Sn-rich and more relaxed. These findings are of practical importance for engineering the light emission properties in GeSn NWs for future optoelectronic applications.

The reliability of the FEM simulations allows us to further correlate the strain relaxation mechanisms and the progressive enrichment in Sn with increasing shell thickness. In contrast to planar films, the axial symmetry of core/shell NWs, even in the case of uniform composition, results in a non-uniform strain field within the shell, with a progressive accommodation of the lattice parameter, moving from the inner interface towards the lateral free surfaces. This is highlighted in Fig. 3a where the variation of the representative strain components along the NW radius ("y" axis), from the core-shell interface to the centre of one facet, is reported for the case of a shell with uniform composition. The calculation parameters are set to match the experimental case of ref. 20 where the gradient in Sn composition is larger. The NW has a Ge core with a radius of 25 nm and a GeSn shell with a thickness of 120 nm and an average composition of 11.7% Sn. In the case of uniform composition, as shown in Fig. 3a, all strain components converge to zero when approaching the NW sidewalls. When Sn-poor (5% Sn) sunburst stripes and a radial compositional Sn gradient (from 9% to 13%) are taken into account, a change in the strain mapping is observed, as illustrated in Fig. 3b. Both the radial and the tangential strain components remain significantly relaxed close to the core-shell interface, but a non-zero

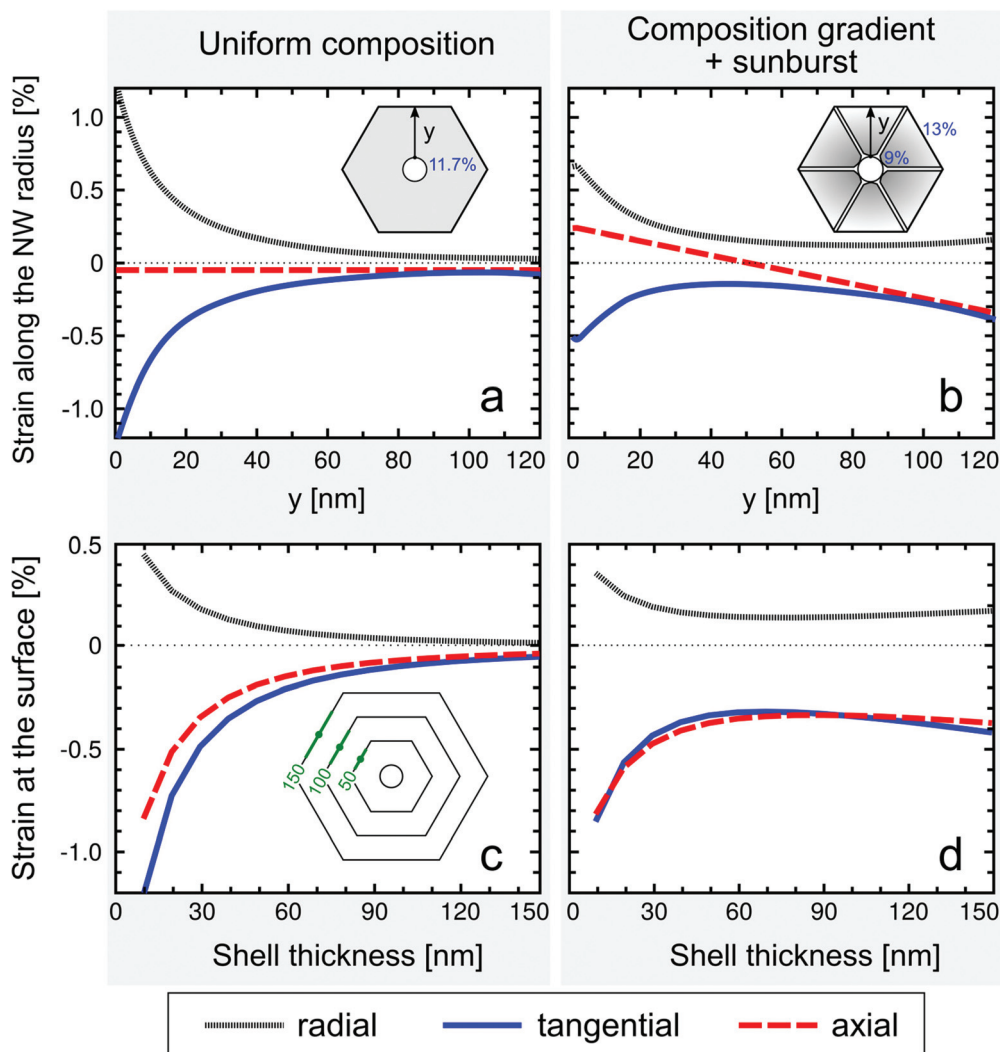


**Fig. 3** Variation of the radial, tangential and axial strain components along the NW radius “ $y$ ” (see insets) obtained by FEM calculations in the case of uniform composition (a) and in the presence of composition gradient and sunburst segregation (b). (c and d) Same comparison for the strain at the surface computed for different thicknesses of the NW shell. The strain values are averaged in the central 1/3 portion of the NW lateral surface, 750 nm far from the NW top. The core radius is 25 nm and the shell is  $\sim$ 120 nm thick. In (b and d) Sn composition varies linearly from 9% to 13%, corresponding to an average of 11.7% as used in (a and c), and 5% Sn sunburst stripes are also taken into account.

strain level is now observed in the outer portion of the shell. In addition, the axial strain is not constant, with a change from tensile to compressive while moving toward the outer portion of the shell. Evidently, the gradual increase of the Sn amount throughout the shell, corresponding to a greater misfit with respect to the pure Ge core, compensates the beneficial effect of the NW geometry in releasing strain (see Fig. 3a).

In order to assess the origin of the grading of the Sn content within the shell, we investigated the variation of the strain at the NW surface (averaged in the centre of the side facet on a surface as wide as 1/3 of the total facet width) for different shell thicknesses, *i.e.* during the lateral growth of the shell. The simulations of the strain at the surface, for a uniform and a graded (including sunburst stripes) Sn compo-

sition, are plotted in Fig. 3c and d. When the uniform composition is considered, all strain components at the surface rapidly decrease as the thickness increases, falling below the 0.2% for a shell about two times thicker than the core diameter. In the case of a graded composition profile, most of the strain relaxation is achieved for relatively thin shells. As the shell thickness becomes comparable to the core diameter, all of the strain components tend to stabilize around a nearly constant value, despite any further thickening of the shell. The persistence of this unrelaxed strain state is not favourable from the point of view of system energetics, so that its origin has to be related to the growth kinetics. Indeed, the fact that the growth of the shell is performed in a large excess of Sn, which aims at the highest possible incorporation grade in the alloy, must be taken into account. The progressive Sn enrich-

ment of the shell observed in the experiments is thus interpreted as balancing the tendency toward incorporating Sn, as forced by the growth conditions, and the need to keep the planar strain of the facet below a critical level. In particular, the lowering of the strain at the surface of NWs of increasing shell thicknesses (see Fig. 3c) makes additional Sn incorporation favourable. According to the analysis of Fig. 3d, a critical strain value of about  $-0.4\%$  for both tangential and axial components, and  $0.2\%$  for the radial one, can be identified. As a consequence, a value of  $-0.4\%$  can be considered as the maximum planar strain on the facet permitting an increment of Sn incorporation above the current Sn concentration. Here, this value is determined for the  $\{112\}$  surface, but as it is essentially determined by the size of the Sn atoms, we believe it to be similar for other surfaces.

## Conclusions

The connection between residual misfit strain and Sn incorporation in core/shell NWs has been analysed quantitatively both by TEM measurements, close to the accuracy limits, and by realistic 3D FEM calculations. The impact on strain relaxation determined by the sunburst segregation of Ge at the NW edges, and by the spontaneous grading of the shell has been studied, indicating a stiffening of the shell with respect to the uniform composition case. More importantly, the strain threshold permitting an incremental Sn incorporation has been predicted to be  $-0.4\%$  for planar strain on the  $\{112\}$  facets of the NW. This corresponds to a mechanism of compositional pulling, similar to the one identified in other systems (typically AlGaIn alloys),<sup>17</sup> but to the best of our knowledge not yet reported for core/shell NWs and in particular for the Ge/GeSn case. Here, the NW configuration is crucial, as the fully elastic relaxation mechanism allows for a quantitative estimation of the critical strain value, an issue that is not possible in the case of planar films with plastic relaxation.

## Methods

### Strain field by Finite Element Method

Strain relaxation in the core/shell NWs is computed by numerical solution of the mechanical equilibrium equations by the Finite Element Method (FEM). The commercial software COMSOL Multiphysics® is used. A realistic, fully three-dimensional representation of the NW structure is taken into account. In particular, a  $5\ \mu\text{m}$  tall NW is modelled. A cylindrical Ge core is assumed, surrounded by a GeSn shell bounded by six  $\{112\}$  facets. The strain field is calculated by solving the mechanical equilibrium problem for inhomogeneous systems. The (bulk) lattice mismatch between the Ge core and the GeSn shell introduces an initial strain (eigenstrain) that is relaxed to the equilibrium condition (non-uniform residual strain), both by a strain transfer from the shell to the core and by the strain relaxation at the free sidewalls. More precisely, the lattice mis-

match is set in the simulations as an initial compressive strain in the GeSn shell, while the Ge core is assumed as the reference undeformed state. The mismatch  $(a_{\text{Ge}} - a_{\text{GeSn}})/a_{\text{GeSn}}$  is defined at each point as a function of the local Sn content  $x$ , using a corrected version of Vegard's law for  $a_{\text{GeSn}} = a_{\text{Ge}}(1 - x) + a_{\text{Sn}}x + b_{\text{GeSn}}x(1 - x)$  with  $a_{\text{Ge}} = 5.657\ \text{\AA}$  and  $a_{\text{Sn}} = 6.489\ \text{\AA}$  the bulk lattice parameters and  $b_{\text{GeSn}} = 0.041\ \text{\AA}$  the bowing parameter.<sup>28</sup> The anisotropic elastic constants for the zinc-blende lattice structure are considered according to ref. 29 and their values are interpolated between those of Ge and Sn by Vegard's law  $C_{\text{GeSn}} = (1 - x)C_{\text{Ge}} + xC_{\text{Sn}}$ , with  $C_{\text{Sn}}^{11} = 69\ \text{GPa}$ ,  $C_{\text{Sn}}^{12} = 29.3\ \text{GPa}$ ,  $C_{\text{Sn}}^{44} = 36.2\ \text{GPa}$ ,  $C_{\text{Ge}}^{11} = 126\ \text{GPa}$ ,  $C_{\text{Ge}}^{12} = 44\ \text{GPa}$ ,  $C_{\text{Ge}}^{44} = 67.7\ \text{GPa}$ . The NW is treated as free-standing, as it actually is for the TEM analysis, by imposing symmetric boundary conditions with respect to the central cross-section.

To better reproduce the experimental evidence and to provide a more quantitative analysis of the strain relaxation, both the Sn-poor sunburst stripes and the progressive increase of Sn content throughout the shell are taken into account. In particular, 8 nm-thin stripes (allowing for sufficient resolution for the FEM calculation), with a fixed 5% Sn concentration, are traced radially from the core to the vertices of the hexagonal cross-section of the NW. Moreover, in order to reproduce the higher Ge content in the region immediately surrounding the core, as recognized in the experiments,<sup>20</sup> the stripes are connected to the core region by small triangles.

### Strain analysis by transmission electron microscopy

Transmission electron microscopy studies were performed using a probe corrected JEOL ARM, operated at 200 kV, equipped with a Centurio 100 mm<sup>2</sup> SDD EDS detector. Calibration of the electron diffraction patterns was done in a 2-step process. Firstly, the anisotropy in the magnification in the diffraction images was quantified. The ED patterns do not have exactly the same magnification in all directions of the image (due to the limitations to the accuracy of the microscope; the anisotropy is instrument dependent). This anisotropy calibration was performed on the ring pattern of a poly-crystalline Au sample. By measuring the radial variation in the radius of the diffraction rings, a roundness of 99.2% was measured. Secondly, Pt nanoparticles were deposited on the supporting holey carbon film prior to depositing the wires on the film to be used as the internal calibration of the absolute values in each diffraction pattern.

## Conflicts of interest

There are no conflicts to declare.

## Acknowledgements

Solliance and the Dutch province of Noord Brabant are acknowledged for funding the TEM facility.

## References

- 1 S. Wirths, D. Buca and S. Mantl, *Prog. Cryst. Growth Charact. Mater.*, 2016, **62**, 1–39.
- 2 S. Wirths, R. Geiger, N. von den Driesch, G. Mussler, T. Stoica, S. Mantl, Z. Ikonik, M. Luysberg, S. Chiussi, J. M. Hartmann, H. Sigg, J. Faist, D. Buca and D. Grützmacher, *Nat. Photonics*, 2015, **9**, 88–92.
- 3 R. Soref, D. Buca and S.-Q. Yu, *Opt. Photonics News*, 2016, **27**, 32.
- 4 M. Paniccia, *Nat. Photonics*, 2010, **4**, 498–499.
- 5 P. Moontragoon, R. A. Soref and Z. Ikonik, *J. Appl. Phys.*, 2012, **112**, 73106.
- 6 N. von den Driesch, D. Stange, S. Wirths, G. Mussler, B. Holländer, Z. Ikonik, J. M. Hartmann, T. Stoica, S. Mantl, D. Grützmacher and D. Buca, *Chem. Mater.*, 2015, **27**, 4693–4702.
- 7 S. Takeuchi, A. Sakai, K. Yamamoto, O. Nakatsuka, M. Ogawa and S. Zaima, *Semicond. Sci. Technol.*, 2007, **22**, S231–S235.
- 8 A. Attiaoui and O. Moutanabbir, *J. Appl. Phys.*, 2014, **116**, 63712.
- 9 R. Soref, *Nat. Photonics*, 2010, **4**, 495–497.
- 10 R. W. Olesinski and G. J. Abbaschian, *Bull. Alloy Phase Diagrams*, 1984, **5**, 265–271.
- 11 G. He and H. A. Atwater, *Appl. Phys. Lett.*, 1996, **68**, 664–666.
- 12 R. Ragan, C. C. Ahn and H. A. Atwater, *Appl. Phys. Lett.*, 2003, **82**, 3439–3441.
- 13 S. Takeuchi, A. Sakai, O. Nakatsuka, M. Ogawa and S. Zaima, *Thin Solid Films*, 2008, **517**, 159–162.
- 14 S. Wirths, D. Buca, G. Mussler, A. T. Tiedemann, B. Hollander, P. Bernardy, T. Stoica, D. Grützmacher and S. Mantl, *ECS J. Solid State Sci. Technol.*, 2013, **2**, N99–N102.
- 15 S. Biswas, J. Doherty, D. Saladukha, Q. Ramasse, D. Majumdar, M. Upmanyu, A. Singha, T. Ochalski, M. A. Morris and J. D. Holmes, *Nat. Commun.*, 2016, **7**, 11405.
- 16 J. Aubin, J. M. Hartmann, A. Gassenq, L. Milord, N. Pauc, V. Reboud and V. Calvo, *J. Cryst. Growth*, 2017, **473**, 20–27.
- 17 H. Y. Lin, Y. F. Chen, T. Y. Lin, C. F. Shih, K. S. Liu and N. C. Chen, *J. Cryst. Growth*, 2006, **290**, 225–228.
- 18 J. Margetis, A. Mosleh, S. Al-Kabi, S. A. Ghetmiri, W. Du, W. Dou, M. Benamara, B. Li, M. Mortazavi, H. A. Naseem, S.-Q. Yu and J. Tolle, *J. Cryst. Growth*, 2017, **463**, 128–133.
- 19 J. Aubin, J. M. Hartmann, A. Gassenq, J. L. Rouviere, E. Robin, V. Delaye, D. Cooper, N. Mollard, V. Reboud and V. Calvo, *Semicond. Sci. Technol.*, 2017, **32**, 94006.
- 20 S. Assali, A. Dijkstra, A. Li, S. Koelling, M. A. Verheijen, L. Gagliano, N. von den Driesch, D. Buca, P. M. Koenraad, J. E. M. Haverkort and E. P. A. M. Bakkers, *Nano Lett.*, 2017, **17**, 1538–1544.
- 21 A. C. Meng, C. S. Fenrich, M. R. Braun, J. P. McVittie, A. F. Marshall, J. S. Harris and P. C. McIntyre, *Nano Lett.*, 2016, **16**, 7521–7529.
- 22 J. Margetis, S.-Q. Yu, N. Bhargava, B. Li, W. Du and J. Tolle, *Semicond. Sci. Technol.*, 2017, **32**, 124006.
- 23 M. Heiss, Y. Fontana, A. Gustafsson, G. Wüst, C. Magen, D. D. O'Regan, J. W. Luo, B. Ketterer, S. Conesa-Boj, A. V. Kuhlmann, J. Houel, E. Russo-Averchi, J. R. Morante, M. Cantoni, N. Marzari, J. Arbiol, A. Zunger, R. J. Warburton and A. Fontcuberta i Morral, *Nat. Mater.*, 2013, **12**, 439–444.
- 24 C. Eckhardt, K. Hummer and G. Kresse, *Phys. Rev. B: Condens. Matter Mater. Phys.*, 2014, **89**, 165201.
- 25 M. Takeda and J. Suzuki, *J. Opt. Soc. Am. A*, 1996, **13**, 1495.
- 26 M. J. Hÿtch, E. Snoeck and R. Kilaas, *Ultramicroscopy*, 1998, **74**, 131–146.
- 27 F. Pezzoli, A. Giorgioni, D. Patchett and M. Myronov, *ACS Photonics*, 2016, **3**, 2004–2009.
- 28 F. Gencarelli, B. Vincent, J. Demeulemeester, A. Vantomme, A. Moussa, A. Franquet, A. Kumar, H. Bender, J. Meersschaut, W. Vandervorst, R. Loo, M. Caymax, K. Temst and M. Heyns, *ECS J. Solid State Sci. Technol.*, 2013, **2**, P134–P137.
- 29 O. Madelung, *Semiconductors: Group IV Elements and III–V Compounds*, Springer-Verlag Berlin Heidelberg, Berlin, Heidelberg, 1991.